Contents lists available at ScienceDirect

Applied Catalysis B: Environmental

Activity and selectivity descriptors for iron carbides in CO_2 hydrogenation

Qingxin Yang [a], Elizaveta A. Fedorova [a], Sergey A. Petrov [b], Jana Weiss [a], Henrik Lund [a], Andrey S. Skrypnik [a], Carsten Robert Kreyenschulte [a], Victor Yu. Bychkov [c], Alexander A. Matvienko [b,d], Angelika Brueckner [a], Evgenii V. Kondratenko [a,*]

[a] *Leibniz-Institut für Katalyse e.V., Albert-Einstein-Str. 29a, 18059 Rostock, Germany*
[b] *Institute of Solid-State Chemistry and Mechanochemistry, Kutateladze Str. 18, 630128 Novosibirsk, Russia*
[c] *Semenov Institute of Chemical Physics, Russian Academy of Sciences, Kosygina Str. 4, GSP-1, 119991 Moscow, Russia*
[d] *Novosibirsk State University, Pirogova Str. 1, 630090 Novosibirsk, Russia*

ARTICLE INFO

ABSTRACT

CO_2 conversion into value-added products provides an attractive way to close carbon cycles and to minimize the dependence on oil-based feedstock. To understand how product distribution in CO_2 hydrogenation can be controlled, as required for purposeful catalyst design, we prepared single-phase α-Fe_2O_3 materials differing in their reducibility due to the different size of crystallites and the presence of planar defects in the iron sublattice. Their structural evolution during reduction and under CO_2 hydrogenation conditions as well as their catalytic and adsorptive properties towards CO, CO_2, and H_2 were elucidated through combining kinetic (spatially resolved), physicochemical and chemisorption analyses. The obtained results suggest that the reducibility of α-Fe_2O_3 is a key factor affecting in situ transformation of this oxide into Fe_5C_2 with planar defects, which seem to determine the generation of surface intermediates from CO, CO_2, and H_2, and accordingly CO_2 hydrogenation to CO exclusively or also CO hydrogenation to hydrocarbons.

1. Introduction

Carbon dioxide (CO_2) utilization has attracted great attention of the academia and the industry due to the possibility to solve both environmental and energy problems.[1,2] In this concept, CO_2 reacts with "green" hydrogen generated from water using renewable energy to produce carbon monoxide[3–6], methanol[7], methane, and higher hydrocarbons[8,9]. Depending on the target product, catalysts based on Fe[10–14], Co[15,16], Ni[17,18], Cu[19,20], or noble metals[21,22] are employed. As CO formed from CO_2 shows higher reactivity than CO_2, it can also participate in further hydrogenation reactions. Thus, a great challenge in CO_2 valorization is controlling product selectivity.

It is possible to switch between CO and CH_4 production over catalysts based on noble metals through tuning the size of supported metal species [23,24], modifying metal-support interactions[25], changing the kind of support[26], or controlling the microstructure of active sites[5]. However, it is difficult to control product selectivity in CO_2 hydrogenation (CO_2-FT) to hydrocarbons over Fe-based materials.[8,27] This is related to the multifaceted reaction network including three main reactions: (i) CO_2 reduction into CO (the reverse water gas shift (RWGS) reaction), (ii)

the hydrogenation of CO to C_{2+}–hydrocarbons (the Fischer-Tropsch reaction, CO-FT), and (iii) CO/CO_2 hydrogenation to CH_4. In addition, the direct CO_2 hydrogenation to hydrocarbons was included into a kinetic model developed by Riedel et al.[28] for a Fe/Al_2O_3/Cu/K catalyst. This pathway plays, however, a minor role in comparison with the CO hydrogenation.

Fe_3O_4 and FeC_x (iron carbides) are considered as active phases in CO_2-FT, with the latter hydrogenating CO to C_{2+}–hydrocarbons.[29,30] The introduction of alkali metals and/or transition metals as promoters for Fe-based catalysts positively influences the formation of FeC_x and therefore favors the selective conversion of CO into C_{2+}–hydrocarbons. [1,8,31] However, the role of iron carbides in the promoted catalysts cannot be unambiguously understood because the promoters can be directly involved in CO_2, CO, and H_2 activation. Our previous statistical analysis of literature data on CO_2-FT revealed that C_{2+}–hydrocarbons can be selectively produced over non-promoted iron oxide catalysts.[32] This statement was recently proven by us, experimentally [33]. We prepared a series of well-defined $Fe_xO_yC_z$ materials through controlled decomposition of iron(II) oxalate without any promoters to obtain certain fractions of Fe_3O_4, FeO, Fe, Fe_3C, and Fe_5C_2 phases. The

---

selectivity to CH_4 could be suppressed to $< 10\%$ at about 25% CO_2 conversion. It remains, however, not fully understood, which physicochemical properties of pure iron(III) oxide influence its reaction-induced transformation into FeC_x and whether the formation of these new phase (s) is the only requirement for achieving high yield of C_{2+}–hydrocarbons. It is also unclear how the ability of FeC_x to activate/adsorb/dissociate CO_2, CO, and H_2 can be controlled to affect catalyst performance.

Motivated by the above challenges, herein, we demonstrate how product distribution in CO_2-FT can be tuned. To avoid any influence introduced by the presence of catalyst support or promoter on structural, physicochemical, and catalytic properties of iron oxides/carbides, we developed pure hematite (α-Fe_2O_3) materials with different crystallite sizes. Our working hypotheses are (i) the reducibility of α-Fe_2O_3 should impose an important effect on the *in situ* formation of Fe-containing phases and (ii) the ability of the latter to generate surface hydrogen species from H_2 and carbon-containing species from CO and CO_2 should be relevant for controlling product selectivity and productivity in CO_2-FT. Furthermore, we analyzed spatial distribution of iron carbides and their reactivity towards adsorption/desorption/dissociation of H_2, CO, and CO_2 as well as towards hydrogenation of carbon oxides to understand their role in the course of CO_2-FT. Finally, the necessity of sophisticated kinetic analysis including surface intermediates for understanding of activity and selectivity relevant factors is highlighted.

2. Experimental section

2.1. Catalyst preparation

The Fe-CP catalyst was prepared through a precipitation method using iron nitrate nonahydrate ($Fe(NO_3)_3 \cdot 9\ H_2O$, AR for Analysis, Fisher Scientific) as precursor and ammonium hydroxide solution (25%, Ph. Eur., Roth) as precipitating agent. Briefly, 20.2 g of $Fe(NO_3)_3 \cdot 9\ H_2O$ was dissolved in 91.2 mL of deionized water followed by stirring for 30 min. Then, a diluted ammonium hydroxide solution (6.7 M) was added dropwise at room temperature under continuous stirring until the value of pH became 9.5. After ageing at the same temperature (3 h), the precipitate was filtered and washed with deionized water to reach the pH value of around 7. The resulting product was dried in a muffle furnace at 100 °C overnight and then calcined at 400, 600 or 700 °C for 6 h at a heating rate of 3 °C min^{-1}. The Fe-SG catalyst was prepared using a sol-gel method. $Fe(NO_3)_3 \cdot 9\ H_2O$, ethylene glycol (99%, Roth) and citric acid (99%, Sigma-Aldrich) at a Fe/ethylene glycol/citric acid molar ratio of 1/1/2 were dissolved in 50 mL of deionized water. After drying at 120 °C overnight, the solid product was calcined in a muffle furnace at 500 °C (with a ramping rate of 3 °C min^{-1}) for 4 h. The Fe-TD catalyst was directly obtained through decomposition of $Fe(NO_3)_3 \cdot 9\ H_2O$ at 600 °C in a muffle furnace with the treatment time of 6 h.

Before starting CO_2-FT tests, the as-prepared catalysts were *in situ* reduced at different temperatures. More details are provided in the section "Steady-state CO_2 hydrogenation catalytic tests". The reduced catalysts are denoted as Fe-x-re y and spent catalysts are named as Fe-x-re y-s, where x indicates the catalyst preparation method (CP, SG, or TD) and y stands for the reduction temperature.

2.2. Catalyst characterization

X-ray diffraction (XRD) powder patterns were recorded using a transmission diffractometer (Stoe Stadi P) equipped with a DECTRIs Mython2 1 K detector and Mo Kα1 radiation (50 kV, 40 mA, 0.70930 Å). The samples were put between two acetate foils before the measurements. HighScore Plus software package (Panalytical) was employed for the fitting of reflection position and pattern by using the Pseudo-Voigt function. The phase analysis was performed using the PDF-2 database (the International Centre of Diffraction Data, ICDD). The crystallite size of α-Fe_2O_3 was determined by applying the Scherrer equation for the

(012), (104), (110), (113), (024), and (116) reflections and an average value is reported. The reflections used for calculating the size of Fe_5C_2 crystallites are (111), (020), (-112), (112), and (021). The Rietveld method was used for the quantitative analysis of crystalline phases. Simulated XRD patterns of α-Fe_2O_3 and Fe_5C_2 phases were obtained with help of VESTA software by using structural data (space group, lattice parameters and atom positions) reported by Schouwink et al.[34] and Retief et al.[35], respectively. The crystal structures were also visualized by the VESTA software.

In situ XRD experiments were conducted using a STOE HT2-*in situ* oven. Herein, a Mython 1 K detector (Debye-Scherrer geometry) was used with a monochromatized Mo Kα_1 radiation (50 kV, 40 mA, 0.70930 Å). Each as-prepared catalyst sample (sieve fraction of 100–150 μm) was filled into a capillary reactor (outer diameter of 2 mm, inner diameter of 1 mm) with a height of about 6 mm. The catalyst bed in the quartz glass capillary was fixed by quartz wool pieces located in the top and bottom catalyst positions. The capillary was placed into the oven and heated in Ar flow (10 mL min^{-1}). The reduction process was monitored using a feed H_2/He (1:1, 10 mL min^{-1}). The individual gas flows were controlled by mass flow controllers (Bronkhorst). The applied temperature correction function was received by observation of well-known phase transitions ($AgNO_3$, $KClO_4$, Ag_2SO_4, SiO_2, K_2SO_4, K_2CrO_4, WO_3, and $BaCO_3$).

Nitrogen adsorption-desorption measurements were carried out using an ASAP 2020 setup (Micromeritics, USA). The specific surface area of catalyst was calculated according to the Brunauer-Emmett-Teller (BET) method. The samples were pre-treated at 250 °C in vacuum for 2 h before starting the measurements.

TGA (thermogravimetric analysis) experiments were conducted at 300 °C using SETSYS Evolution 16/18 (Setaram) apparatus. Each as-prepared catalyst sample (20 mg) was placed into a cup located in the balance. After the system was evacuated, the cup was heated up to 300 °C (10 °C min^{-1}) in He (20 mL min^{-1}) until the mass was unchanged. Finally, a gas mixture of 50 vol% H_2/He (32 mL min^{-1}) was fed and the changes in sample mass were monitored.

H_2 temperature-programmed reduction (H_2-TPR) experiments were carried out in an in-house-made setup. 15 mg of fresh catalyst were heated to 300 °C in Ar flow (10 mL min^{-1}) and kept for 2 h. After cooling down to 50 °C in Ar, the dehydrated catalyst was heated to 900 °C (10 °C min^{-1}) in a mixture of 5 vol%H_2/Ar (10 mL min^{-1}). The signals at m/z of 2, 18, and 40, standing for H_2, H_2O and Ar, respectively, were recorded by an online mass spectrometer (Pfeiffer Vacuum OmniStar GSD 320).

X-ray photoelectron spectroscopy (XPS) experiments were carried out on an ESCALAB 220iXL apparatus (Thermo Fisher Scientific) equipped by a mono-chromated Al Kα radiation (1486.6 eV). The sample was prepared on a stainless-steel holder with conductive double-sided adhesive carbon tape. The electron binding energy was obtained after charge compensation through a flood electron source and was referenced to the C 1 s core level at 284.8 eV.

Mössbauer spectra were recorded at room temperature using an NZ-640 spectrometer (Hungary) with ^{57}Co in a matrix of metallic rhodium. Each experiment was performed in a constant acceleration mode. The isomer shift (IS) was referenced to the metallic α-Fe. An in-house developed program was applied to deconvolute the spectra into the Lorentzian functions.

Scanning transmission electron microscopy (STEM) images were collected using a probe aberration corrected JEM-ARM200F (JEOL) equipped with high angle annular dark field (HAADF), annular dark field (ADF) and annular bright field (ABF) detectors. For chemical analysis and mapping, the microscope has been attached with a Dry SD60GV (JEOL) energy dispersive X-ray spectrometer (EDXS) and an Enfinium ER (Gatan) electron energy loss spectrometer (EELS). EELS elemental maps have been calculated from spectrum imaging data sets by using model spectra of the respective elements for pixelwise fitting using Digital Micrograph 3.4 (Gatan). The STEM characterization and

EELS examination were performed using the *ex situ* manner. To minimize/avoid oxidation of spent catalysts, they were cooled down to room temperature in nitrogen prior to their removal from the reactors.

X-ray absorption spectroscopy (XAS) was applied in transmission mode at the Fe K edge at PETRA III (P65 beamline, DESY Germany). The X-ray absorption near-edge structure (XANES) spectra were normalized, and the extended X-ray absorption fine structure spectra (EXAFS) background was subtracted by using the Athena program (IFFEFIT software package). The k^2-weighted EXAFS were transformed with Fourier function in the k range of 2–12.3 Å^{-1} and multiplied by a Hanning window with sill size of 1 Å^{-1}. Artemis software was used for EXAFS fitting process. The Fourier transformation of EXAFS oscillations was carried out in the k-range of 3.0–11.5 Å^{-1}. The fitting r-range was 1.0–3.5 Å for Fe-CP-re300-s, Fe-TD-300-re300-s, and Fe-CP-re400-s and 1.0–3.0 for Fe-TD-re400-s and Fe_5C_2 reference samples with k^1, k^2 -weight. The amplitude reduction factor (S_0^2) was obtained by fitting the Fe foil reference spectra. The values $S_0^2 = 0.5$ for the Fe-x-re400-s and Fe_5C_2 samples, and $S_0^2 = 0.6$ for Fe-x-re300-s samples were fixed in the refinement.

Temperature-programmed desorption experiments with CO_2 (CO_2-TPD) or CO (CO-TPD) were performed in the setup applied for the above-described H_2-TPR experiments. The amount of catalyst was 50 mg for reduced or spent catalysts in CO_2-TPD experiments or 15 mg in CO-TPD measurements with spent catalysts. Each catalyst sample was heated to 300 °C (10 °C min^{-1}) in Ar with a flow rate of 10 mL min^{-1} and kept for 2 h. Hereafter, the dehydrated sample was cooled down to 50 °C in Ar. The reduction pre-treatment of as-prepared iron oxide materials was performed using the same conditions as applied before CO_2-FT reaction to obtain the reduced catalysts for CO_2-TPD experiments. CO_2 or CO was introduced into the reactors at 50 °C for adsorption until there is no changes in the MS signals of CO_2 or CO. After that, CO_2 or CO was replaced by Ar to remove physically adsorbed CO_2 or CO. The sample was heated in Ar to 800 °C (10 °C min^{-1}). The signals of Ar, CO_2, and CO at m/z of 40, 44, and 28, respectively, were detected by an online mass spectrometer (Pfeiffer Vacuum OmniStar GSD 320).

H_2-D_2 exchange measurements with spent catalysts were carried out at 300 °C. Each catalyst (15 mg) was loaded into a quartz glass reactor and pre-treated in Ar flow (10 mL min^{-1}) at 300 °C for 30 min. Hereafter, the gas mixture D_2/H_2/Ar (2.5 vol%: 2.5 vol%: 95 vol%, 5 mL min^{-1}) was introduced into the reactor. HD was recorded at m/z of 3 by an online mass spectrometer (Pfeiffer Vacuum OmniStar GSD 320). To ensure that the detected HD was really formed through an exchange reaction between H_2 and D_2 on the surface of catalyst, a blank experiment without any catalyst was also carried out. In this way, the real HD concentration formed over the catalyst was obtained by subtracting the background concentration determined in the blank test.

Temperature-programmed hydrogenation of spent catalysts with H_2 (TPH) was conducted in the same apparatus that was employed for the H_2-TPR experiments. In general, 50 mg of each spent catalyst were loaded into a quartz glass reactor. All samples were initially pre-treated in Ar (10 mL min^{-1}) at 300 °C for 2 h with a heating rate of 10 °C min^{-1}. After that, the reactors were cooled down to room temperature in Ar followed by feeding a gas mixture of 5 vol% H_2/Ar (10 °C min^{-1}) and heating the reactor to 900 °C (10 °C min^{-1}). The catalysts were kept at 900 °C for at least 90 min. CH_4 formed during TPH experiments was monitored at m/z of 15 by an online mass spectrometer (Pfeiffer Vacuum OmniStar GSD 320).

In situ Fourier-transform infrared spectroscopy experiments were conducted on a Nicolet iS10 infrared spectrometer. A mercury cadmium telluride (MCT) detector and an in-house-developed high-pressure FTIR cell were employed. The spectra were obtained in transmission mode with a resolution of 4 cm^{-1} and scans of 64. Briefly, catalyst powder (50 mg) was pressed into a wafer (20 mm diameter). Firstly, the sample was *in situ* reduced at 400 °C using a flow of 50 vol%H_2/He mixture for 2 h in the FTIR cell. After that, the catalyst was exposed to reaction atmosphere (CO_2: H_2: He = 1: 3: 1, 50 mL min^{-1} of total flow rate) at 250 °C and 15

bar. A background FTIR spectrum was obtained before the catalyst was exposed to the reaction atmosphere. The final spectra were derived by subtracting the background spectrum.

Raman micro-spectroscopic measurements were carried out using a Renishaw inVia Raman microscope. During the *ex situ* Raman measurements, a spatula tip of the catalyst was put on a microscope slide. 633 nm laser light was employed and the laser power of 0.17–1.7 mW. To conduct *in situ* Raman experiment, a Linkam reaction cell was used. 40–50 mg of the catalyst was loaded into this cell with a height of around 4 mm. The gas flow was controlled by mass flow controllers (Bronkhorst).

2.3. Steady-state catalytic CO_2 hydrogenation tests

CO_2 hydrogenation tests were carried out in an in-house developed setup equipped with 51 fixed-bed stainless-steel tube reactors (276 mm in length with outer and inner diameters of 6 and 4 mm, respectively) in parallel. The total feed flow was equally distributed among the reactors. The flow rate passed through each rector was measured before each experiment. Briefly, the catalyst (300 mg, 250–450 μm fraction) was loaded within the reactor isothermal zone. The resulting catalyst bed is around 1.7 cm in height. For calculating the segmental rates of CO_2 conversion and product formation, different catalyst amounts (50, 20, 10, 5 and 3 mg) were used. For all catalyst amounts, 700 mg of SiC (ESK, 500–710 μm fraction, 2.6 cm in height) were loaded on top of the catalyst particle to ensure a plug flow passing through the catalyst bed and to preheat feed gases. Prior to CO_2-FT reaction, the catalysts were reduced *in situ* at a certain temperature (300, 400, or 500 °C) and 15 bar in a flow (12 mL min^{-1}) of H_2/N_2 = 1/1 mixture for 2 h followed by changing this flow to N_2 flow. After the reactors were cooled down to the reaction temperature in N_2, the feed mixture (H_2/CO_2/N_2 = 3/1/0.3) was introduced. N_2 was used as internal standard gas in gas-chromatographic analysis.

An on-line Agilent 7890 A gas chromatograph containing a flame ionization detector (FID) and a thermal conductivity detector (TCD) was used to identify and quantify the feed components and the reaction products. HP Plot/Q (for CO_2) and MolSieve 5 A (for H_2, N_2, and CO) columns were connected to TCD. AL/S and FFAP columns were connected to FID to analyze C_1–C_8 and C_9–C_{18} hydrocarbons, respectively. All stainless-steel lines between the reactor outlet and the GC inlet were heated to around 180 °C. Eqs. (1) and (2) were used to calculate CO_2 conversion and product selectivity, respectively. The rate of CO_2 conversion into C_{2+}–hydrocarbons was calculated according to Eq. (3).

$$X(CO_2) = 1 - \frac{\dot{n}_{CO_2}^{out}}{\dot{n}_{CO_2}^{in}} \tag{1}$$

$$S(i) = \frac{a_i \dot{n}_i^{out}}{\sum_{i=1}^{n} a_i \dot{n}_i^{out}} \tag{2}$$

$$r_{C_{2+}} = \frac{F_{feed} \cdot \frac{p(CO_2)}{P_{(total)}} \cdot X(CO_2) \cdot S(C_{2+})}{V_m \cdot m_{cat}} \tag{3}$$

where $\dot{n}_i$ with superscripts "*in*" and "*out*" represents molar flows of components at the reactor inlet and outlet, respectively. N_2 was used as an internal standard to consider the reaction-induced changes in the number of moles. F_{feed} is the flow rate of feed gas (mL h^{-1}), $P_{(total)}$ stands for the total pressure, $p(CO_2)$ denotes CO_2 partial pressure, and V_m is the molar volume.

The segmental rates of overall CO_2 consumption ($r(CO_2)$) and CO_2 conversion into a certain reaction product (r_i) were calculated according to Eq. (4).

$$r(CO_2) = \frac{\dot{n}_{CO_2}^a - \dot{n}_{CO_2}^{a+1}}{m^{a+1} - m^a} \ or \ r_i = \frac{\dot{n}_i^{a+1} - \dot{n}_i^a}{m^{a+1} - m^a} \tag{4}$$

where *ṅ* and *m* stand for CO_2, CH_4 or C_{2+}–hydrocarbons molar flow in the reactor outlet and catalyst mass, respectively. *a+ 1* or *a* are used to represent the layers in the catalyst bed.

2.4. Steady-state isotopic transient kinetics analysis (SSITKA)

More details on the SSITKA reactor system used in this work has been introduced in detail in a previous publication[36]. A fresh catalyst sample (50 mg) was initially reduced at 400 °C and 15 bar in a gas mixture of H_2/N_2 (1:1, 12 mL min^{-1}) for 2 h, followed by cooling down to 300 °C in Ar (10 mL min^{-1}). Moreover, the pressure was decreased to 1.5 bar. At 300 °C, Ar flow was replaced by the reaction feed (1CO_2/11 H_2/7Ar) with a GHSV of 36,000 mL g$_{cat}^{-1}$ h^{-1}. After the time on stream of 1.5 h, this feed was replaced by a $^{13}CO_2/H_2/He/Ar$ feed. After the steady state operation was achieved with this feed, a back-switching to the non-labelled feed (1CO_2/11 H_2/7Ar) was carried out. An online gas chromatograph (Agilent 7890 A) and online quadrupole mass spectrometer (Balzers Omni Star) were used for the analysis of feed components and the reaction products. More details on quantitative analysis can be found in section "Steady-state catalytic CO_2 hydrogenation tests". The lifetime of surface intermediates was derived from the area under the corresponding normalized transients considering the inert tracer He for gas-phase holdup correction.[37]. Eq. (5) was used to calculate the number of surface intermediates (N_i).

$$N_i = \frac{F_{i,out}}{m_{cat}}\tau_i \tag{5}$$

where, $F_{i,out}$ is the molar flow rate of product *i* in the reactor outlet, m_{cat} stands for the mass of catalyst.

3. Results and discussion

3.1. General physico-chemical characteristics of as-prepared α-Fe₂O₃ materials

Single-phase α-Fe_2O_3 (the hematite phase (ICDD 01–072–0469), Fig. S1) materials were synthesized through precipitation (CP), sol-gel (SG), and thermal decomposition (TD) methods using iron nitrate as precursor (Fig. 1a). The average crystallite size calculated from X-ray diffraction (XRD) data according to the Scherrer equation is 15 nm for Fe-CP, 25 nm for Fe-SG, and 30 nm for Fe-TD. The specific BET surface area decreases accordingly (Table S1). As proven by scanning transmission electron microscopy (STEM), the particle size of α-Fe_2O_3 is between 15 and 200 nm (Fig. S2 and the corresponding note). Due to the agglomeration of Fe_2O_3 particles, the aggregate/particle size of Fe_2O_3 determined from STEM images is considerably larger than the Fe_2O_3 crystallite size calculated by XRD patterns for all three samples. Fe-CP possesses the smallest Fe_2O_3 crystallite and particle sizes in comparison with Fe-SG and Fe-TD.

The below analysis of XRD data suggests that the as-prepared α-Fe_2O_3 materials differ in defects within the iron sublattice of the hematite structure. As seen in Fig. S1b, the experimental and theoretical XRD patterns do not significantly diverge in the position of the reflection (110), while there are differences in the position of the reflections (012) and (104). In comparison with the XRD patterns of Fe-SG, Fe-TD, and ideally structured α-Fe_2O_3, these reflections in the experimental XRD pattern of the Fe-CP sample are shifted to low 2θ angles. Such shift suggests an increase in the lattice parameter in *c* direction in the hematite crystal structure (Fig. S1c). Disparate shifts in the reflections related to *a*, *b*, and *c* directions in the pattern of previously tested SiC were explained by the presence of planar defects, e.g., packing disorders. [38] The shift in the position of the reflections (110) and (012) in the
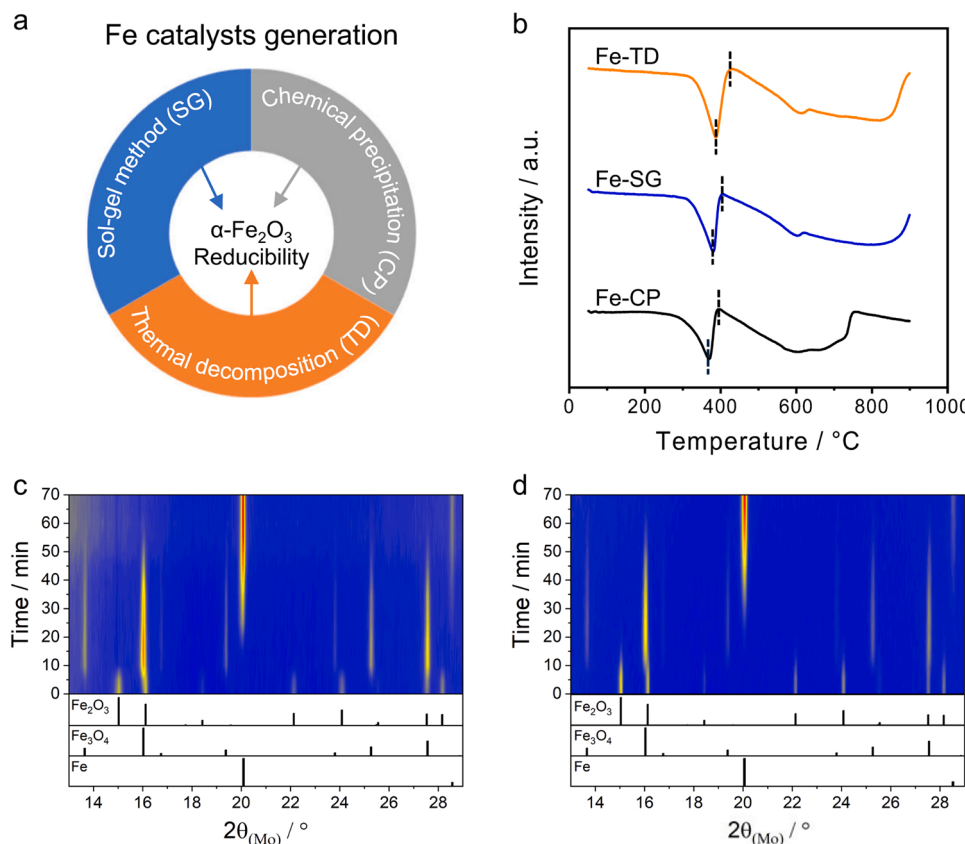

Fig. 1. (a) An introduction to catalyst synthesis methods. (b) The profiles of H_2 outlet concentration in H_2-TPR tests with fresh α-Fe_2O_3. Heatmap of *in situ* XRD patterns collected upon reductive treatment of (c) Fe-CP or (d) Fe-TD in $H_2/He = 1/1$ flow (10 mL min^{-1}) at 1 bar and 300 °C.

patterns of our α-Fe$_2$O$_3$ materials is especially pronounced for the Fe-CP sample (Fig. S1). Another significant difference in the XRD patterns of as-prepared α-Fe$_2$O$_3$ materials is the ratio of the intensities of the reflection and (110) (Fig. S1b). This ratio must be higher than 1 for an ideally structured α-Fe$_2$O$_3$. This is the case for the Fe-TD and Fe-SG samples. Contrarily, this ratio for the Fe-CP sample is close to 1. According to literature[39–41], the low ratio is characteristic of a defective crystalline hematite structure possessing packing disorders in the sublattice of iron along c direction (Fig. S1c). Such anisotropic peak broadening caused by planar defects/faults was not present in Fe-TD and Fe-SG diffraction data. In addition, the fresh Fe-CP and Fe-TD materials do not seem to differ in surface oxygen defects strongly (Fig. S3).

H$_2$ consumption over as-prepared catalysts in H$_2$-TPR tests is characterized by the reduction of α-Fe$_2$O$_3$ to Fe$_3$O$_4$ between 250 and 450 $^\circ$C and the reduction of Fe$_3$O$_4$ to FeO or/and Fe at higher temperatures (Fig. 1b). The temperature of the maximal rate of the reduction of Fe$_2$O$_3$ to Fe$_3$O$_4$ (T$_{max,I}$) for Fe-CP, Fe-SG, and Fe-TD is 372, 381, and 386 $^\circ$C, respectively. While the corresponding onset temperature (T$_{on,II}$) of Fe$_3$O$_4$ reduction is 395, 406 and 432 $^\circ$C. Thus, all reduction processes leading from Fe$_2$O$_3$ to metallic Fe proceed faster with a decrease in the size of Fe$_2$O$_3$ crystallites. To corroborate this statement and to exclude any effect of preparation method (CP, SG, or TD), we also investigated reducibility of Fe-CP prepared at different calcination temperatures to obtain α-Fe$_2$O$_3$ with different size of crystallites. Both the T$_{max,I}$ and T$_{on,II}$ values shift to higher temperatures with an increase in the crystallite size (Table S1). Additional temperature-gravimetric analysis in H$_2$ supports this conclusion (Fig. S4).

According to *in situ* XRD analysis, α-Fe$_2$O$_3$ is quickly converted into Fe$_3$O$_4$ (Fig. 1c, d). This process is faster for Fe-CP than for Fe-TD as concluded from the time for reaching the maximal fraction of Fe$_3$O$_4$ (15 min *vs.* 24 min, Fig. S5). No metallic Fe was detected until this process completed. Thus, α-Fe$_2$O$_3$ is not directly reduced to Fe. The fraction of Fe$_3$O$_4$ diminishes with a further increase in time on H$_2$ stream because of the conversion of Fe$_3$O$_4$ into Fe. The rate of α-Fe$_2$O$_3$ reduction to Fe$_3$O$_4$ is higher than the rate of Fe formation from Fe$_3$O$_4$. *In situ* Raman studies proved this conclusion (Fig. S6). The above-discussed results (H$_2$-TPR, TGA, *in situ* XRD, and *in situ* Raman) evidence that the rates of individual pathways in the course of Fe$_2$O$_3$ reduction to Fe increase with a decrease in the size of Fe$_2$O$_3$ crystallites. Such size-reducibility relationship agrees with previous studies dealing with TiO$_2$[42] or monoclinic ZrO$_2$[43] differing in the size of crystallites.

3.2. Affecting product selectivity in CO$_2$ hydrogenation

To check if the reducibility of α-Fe$_2$O$_3$/Fe$_3$O$_4$ influences catalytic performance of iron carbides *in situ* formed in CO$_2$-FT, we performed CO$_2$ hydrogenation tests at 350 $^\circ$C and 15 bar using as-prepared α-Fe$_2$O$_3$ materials, which had been reduced in 50 vol% H$_2$ in N$_2$ at 300, 400, or 500 $^\circ$C in same setup and at same pressure before starting the hydrogenation reaction. Regardless of the reduction temperature, Fe-CP reveals the selectivity to CO, CH$_4$, and C$_{2+}$–hydrocarbons of about 21%, 33%, and 46%, respectively, at CO$_2$ conversion of around 30% (Fig. 2a). Fe-SG and Fe-TD reduced at 400 or 500 $^\circ$C perform similarly to Fe-CP. However, they reach a near to 100% CO selectivity without a strong decrease in CO$_2$ conversion, when they have been reduced at 300 $^\circ$C (Fig. 2a). This means that the RWGS reaction takes place, but any CO/CO$_2$ hydrogenation reactions are near to completely suppressed even at 15 bar. The CO-FT reaction (the formation of hydrocarbons) is actually favored by elevated pressure. For example, Galvis et al.[44] reported that the conversion rate of CO over supported Fe catalysts at 20 bar was around ten times as high as that achieved at 1 bar.

On-stream stability of the catalysts reduced at different temperatures was also studied. A slight decrease in CO$_2$ conversion and an increase in CO selectivity with rising time on reaction stream were observed over Fe-CP (Fig. S7a, d). No significant changes were determined for Fe-SG and Fe-TD regardless of catalyst reduction temperature (Fig. S7b, c, e,
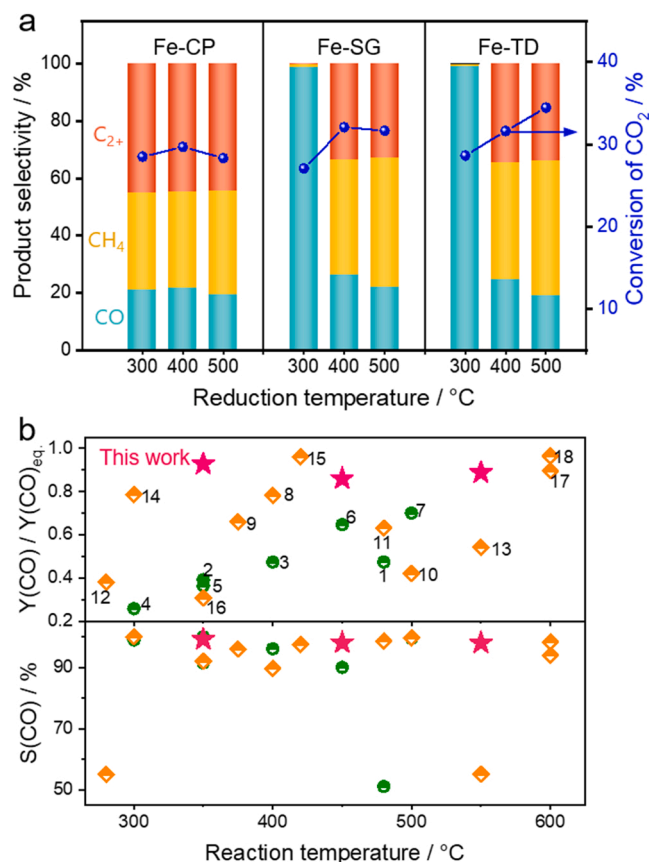

Fig. 2. (a) The conversion of CO$_2$ and product selectivity in CO$_2$-FT over Fe-CP, Fe-SG, and Fe-TD after 10 h on stream at 350 $^\circ$C and 15 bar using a feed H$_2$/CO$_2$/N$_2$ = 3/1/0.3 (modified contact time of 1160 mL g$_{cat}^{-1}$ h^{-1}). The catalysts were reductively (15 bar, H$_2$/N$_2$ = 1/1, 2 h) treated at 300, 400, or 500 $^\circ$C before starting the CO$_2$-FT reaction. (b) The selectivity to CO and the Y(CO)/Y(CO)$_{eq}$ ratio obtained over Fe-TD reduced at 300 $^\circ$C and the state-of-the-art catalysts. Green circles correspond to noble metal-based catalysts, orange diamonds correspond to non-noble metal-based catalysts, and the catalysts reported in this work were labeled by asterisks. (1) 0.1Ru/Al$_2$O$_3$ (ref.[23]); (2) K80-Pt/L (ref.[4]); (3) 8-Pt/Au@Pd@1Co (ref.[21]); (4) 5Ir/Ce (ref.[25]); (5) Rh@S-1 (ref.[5]); (6) Pd/BNCT (ref.[22]); (7) 0.02 wt% Pt/Fe$_3$O$_4$ (ref.[12]); (8) Fe-Cu/Al$_2$O$_3$ (ref.[10]); (9) TiFe/C (ref.[11]); (10) Fe$_3$O$_4$ (ref.[12]); (11) Fe$_3$O$_4$ (ref.[13]); (12) 20Fe (ref.[14]); (13) 3 wt% Ni/Ce-Zr-O (ref.[18]); (14) SCuCe-re (ref.[20]); (15) 7.4Ni/ZIF-8-C (ref.[17]); (16) Co$_3$O$_4$-2 h (ref.[16]); (17) BaCe$_{0.2}$Zr$_{0.6}$Y$_{0.16}$Zn$_{0.04}$O$_3$ (ref.[3]); (18) P-K-Mo$_2$C/γ-Al$_2$O$_3$ (ref.[6]). Feed composition, reaction temperature, and GHSV of all tested catalysts including Fe-TD from the present study are provided in Table S2.

and f). Therefore, the reduction-dependent performance in Fig. 2a is not affected by catalyst stability. Additional results presented and discussed in the below sections provide fundamentals behind the effects of the size of α-Fe$_2$O$_3$ crystallites and the kind of reductive catalyst treatment on the changes in product selectivity of CO$_2$-FT.

To elucidate the potential of Fe-TD in CO production from CO$_2$, additional catalytic tests were carried out. The fresh catalyst was initially reduced at 300 $^\circ$C in 50 vol% H$_2$ in N$_2$ and then applied for CO$_2$ hydrogenation at atmospheric pressure and different reaction temperatures (Fig. S8). An increase in CO$_2$ conversion from 12.5% to 49.4% is observed when the temperature is increased from 350 to 550°C, while the selectivity to CO is not influenced and above 98%. We also compared this catalyst with the state-of-the-art RWGS catalysts in terms of CO production (Table S2). As a criterion, we used the ratio of the experimental yield of CO to the thermodynamically possible yield (Y(CO)/Y(CO)$_{eq}$) and the experimental CO selectivity. Our catalyst shows unexpectedly high (>98%) CO selectivity (Fig. 2b, Table S2) at above 86%

equilibrium CO_2 conversion.

3.3. Carbon-containing species on the surface of spent catalysts

As surface carbon-containing species could have a pronounce effect on product selectivity in CO_2-FT reaction over different catalysts, we analyzed spent catalysts (reduced at 300 or 400 °C prior to CO_2-FT) by temperature-programmed hydrogenation (TPH) in H_2. The corresponding materials are abbreviated as Fe-x-re300-s or Fe-x-re400-s (x = CP, TD, or SG). CH_4 was formed over all catalysts. This result proves that surface carbon-containing species formed in the course of CO_2-FT were hydrogenated by H_2 to CH_4 (Fig. 3a–c, Table S3). The assignment of different carbon-containing species on spent catalysts which led to the formation of CH_4 at different temperatures is summarized in Table S3. CH_4 formation with the peak located below 300 °C (α) originates through a reaction of H_2 with adsorbed atomic carbon or/and surface carbon. While the peak located at 350–450 °C (β) is related to the hydrogenation of polymeric or/and amorphous carbon aggregates. [45] The α species are exclusively characteristic for Fe-CP-re400-s. Moreover, all spent Fe-CP should be different from all spent Fe-SG and Fe-TD regarding the β species because CH_4 formed over the Fe-CP spent catalysts appears at much lower temperatures (Fig. 3a–c). Fe-TD-re400-s displays an additional CH_4 peak (510 °C) which is due to the hydrogenation of polymeric carbon with high stability.

The hydrogenation of Fe_5C_2 results in a well-resolved CH_4 peak at 530 °C (γ₁) for Fe-CP-re400-s.[45] Such species on the surface of Fe-SG-re400-s and Fe-TD-re400-s are less reactive because they are hydrogenated at higher temperatures. It can be clearly seen that γ₁ peak in the TPH profiles of Fe-SG-re400-s and Fe-TD-re400-s is located at a broader temperature range, suggesting that the Fe_5C_2 species on these catalysts are more heterogeneous in their morphology/nanostructure (Fig. 3b, c). Moreover, an additional peak (γ₂) is present in the TPH profiles of these two catalysts. This species should be Fe_3C as discussed below. Importantly, Fe_5C_2 in Fe-SG-re300-s and Fe-TD-re300-s is hydrogenated at higher temperatures in comparison with the Fe-SG-re400-s and Fe-TD-re400-s catalysts. This result suggests that the poor ability of Fe-TD-re300-s and Fe-SG-re300-s to hydrogenate CO/CO₂ in CO_2-FT tests (Fig. 2a) can be related to the low reactivity of Fe_5C_2 to interact with H_2.

CH_4 formation above 690 °C results from the hydrogenation of graphitic deposits[46]. The lowest amount of such deposits was determined for the spent Fe-CP catalysts. The results of Raman tests with the same spent catalysts support this conclusion (Fig. S9). The bands at 1585 cm^{-1} and 1325 cm^{-1} characteristic of carbon deposits[47] are much stronger in the spectra of Fe-SG-re400-s and Fe-TD-re400-s than those in the spectrum of Fe-CP-re400-s.

3.4. Fe-containing phases in reduced or spent catalysts

All catalysts reduced at 300 and 400 °C are composed of Fe_3O_4 and Fe (Fe-x-re300/400, x = CP, SG, or TD, Table S4). No correlation between the crystallite size of as-prepared Fe_2O_3 and that of obtained Fe/Fe_3O_4 could be established (Table S5). Fe content increases, however, with increasing reduction temperature and correlates with Fe_2O_3 reducibility.

Regardless of the size of α-Fe_2O_3 crystallites and the reduction temperature before CO_2-FT, metallic Fe is not present in all spent catalysts. The Fe-CP-based spent catalysts (Fe-CP-re400-s and Fe-CP-re300-s) are comprised of Fe_5C_2 and Fe_3O_4 (Fig. 3d, e; Fig. S10). As the content of these compounds is not influenced by catalyst reduction temperature applied before CO_2-FT, no difference in the performance of differently reduced Fe-CP could be established (Fig. 2a).

Fe_5C_2, Fe_3O_4, and Fe_3C were determined in Fe-SG-re400-s and Fe-TD-re400-s (Fig. 3d, e; Fig. S11). The presence of Fe_3C is probably due to the low reducibility of fresh Fe-SG and Fe-TD (Fig. 1d, Figs. S4–6). Low oxygen removal ability is harmful to carbon permeation, and

consequently favors the formation of carbon-less Fe_3C rather than Fe_5C_2[48]. The concentration of the carbides in Fe-SG-re400-s and Fe-TD-re400-s is higher in comparison with that of Fe-CP-re400-s (Fig. 3e). Fe_3O_4 and Fe_5C_2 are the only phases detected in Fe-SG-re300-s and Fe-TD-re300-s. However, the concentration of Fe_5C_2 in these samples is lower than in their counterparts reduced at 400 °C, i. e., 4.6% vs. 10.8%, and 6.1% vs. 14.7% (Fig. 3e, Fig. S10).

To further understand the reaction-induced catalyst restructuring, the composition of spent catalysts Fe-CP-re400-s and Fe-TD-re400-s was also analyzed in a space-resolved manner. To this end, we filled reactor for CO_2 hydrogenation tests with 300 mg of fresh catalyst (Fe-CP or Fe-TD) composed of 6 segments (Fig. 3f). The two adjacent segments are separated by a layer of quartz wool. The catalysts were reduced at 400 °C and then directly tested in CO_2-FT under the same conditions as in Fig. 2a. Fe_3O_4 and Fe_5C_2 are present in the first two upstream located layers of Fe-TD-re400-s according to Mössbauer and XRD analysis (Figs. S12, 13). The corresponding Fe_5C_2 fractions are 85.2% and 73.8% (Fig. 3 f). These values are higher than 50.0% and 18.1% for Fe-CP-re400-s. The remaining downstream-located layers of Fe-CP-re400-s catalyst bed contain Fe_3O_4 exclusively. The lower concentration of Fe_5C_2 in Fe-CP-re400-s can be explained by the fact that the carbide structure possesses planar defects (see below). The defective Fe_5C_2 seems to be easily oxidized to Fe_3O_4 under CO_2 hydrogenation conditions. The second and third upstream-located layers of Fe-TD-re400-s contain about 7.7% and 41.7% of Fe_3C, respectively. Fe_3O_4 was the only component in the remaining downstream-located catalyst layers. The formation of Fe_3C in Fe-TD-re400-s should be related to the changes in the concentrations of CO, H_2, CO_2, and H_2O along the catalyst bed. These changes affect the kinetics of iron oxides reduction and metallic iron carburization, leading to a preferential formation of Fe_3C.

To check if Fe_5C_2 formed in situ from Fe-CP, Fe-TD, and Fe-SG differs in its structural characteristics, we analyzed XRD patterns of spent catalysts located in the first 6.7% upstream-located layer, which is enriched by the iron carbide phase (Fig. S14, 15). Similar to the XRD patterns of fresh α-Fe_2O_3, there is no difference in the position of the most intensive reflection (510) in the patterns of Fe-CP-re300-s, Fe-TD-re300-s, Fe-SG-re300-s, Fe-CP-re400-s, Fe-TD-re400-s, Fe-SG-re400-s, and the ideal Fe_5C_2. A shift in the position of the reflections (40−2) and (31−2) was established for the Fe-CP spent catalysts (Fig. S14b, S15b). It should be related to the presence of planar defects/faults in the iron sublattice along c direction (Fig. S14c). Importantly, the same defective structure was also identified in fresh Fe-CP catalyst (Fig. S1c). On this basis it can be assumed that the imperfectness of the α-Fe_2O_3 structure is somehow preserved in the structure of the therefrom generated Fe_5C_2.

According to transmission electron microscopic analysis, Fe-CP-re400-s and Fe-TD-re400-s reveal a similar core-shell structure (Fig. S16, 17). As proven by EELS elemental mapping, oxidic iron and oxygen are mainly enriched in the shell part, while carbidic iron and carbide species are predominant in the core (Fig. S16i, 17i). There is no difference between the distribution of iron oxide and iron carbide in a level of particle. The conclusion about the phase distribution is also supported by the EELS data of C and O at different regions of a particle (Fig. S16e-g, S17e-g). Fe-CP-re300-s and Fe-TD-re300-s are predominantly comprised of iron oxide particles and few iron carbide particle (Fig. S18, S19). There is no obvious difference in the morphology of particles in these samples compared with Fe-CP-re400-s and Fe-TD-re400-s.

3.5. Local structural characteristics of iron in spent catalysts

X-ray absorption spectroscopy (XAS) was used to analyze local structure and chemical state(s) of iron in the first top layer of spent Fe-CP and Fe-TD catalysts, where Fe_5C_2 is present in the highest concentration. Fig. 3 g shows the Fe K-edge X-ray absorption near edge structure (XANES) spectra of Fe-CP-re400-s and Fe-TD-re400-s, while the corresponding data for Fe-CP-re300-s and Fe-TD-re300-s are presented
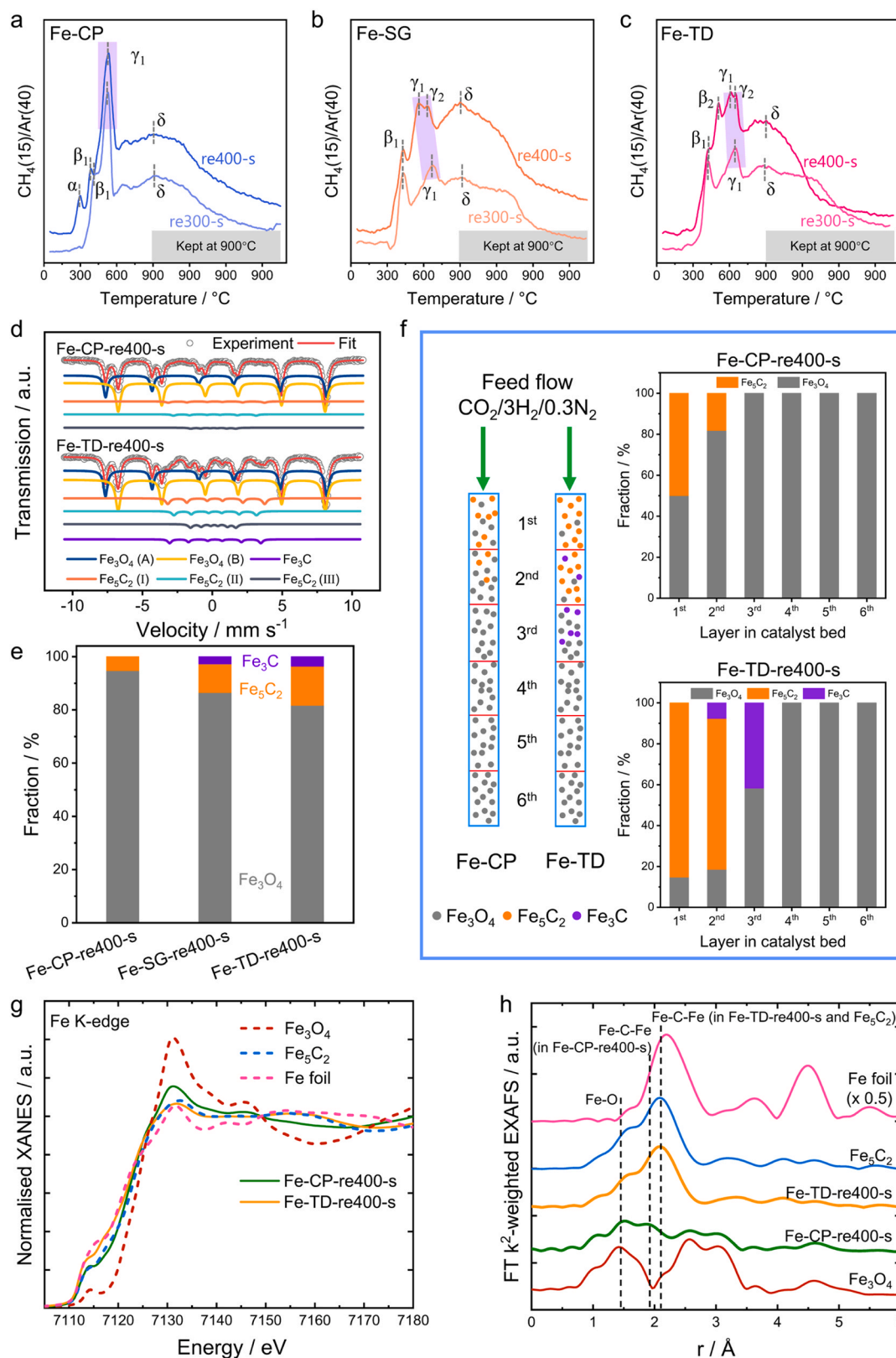
Fig. 3. Profiles of CH_4 formation in temperature-programmed hydrogenation (TPH) tests (5 vol% H_2 in Ar flow) with spent (a) Fe-CP, (b) Fe-SG, and (c) Fe-TD catalysts after CO_2-FT reaction with preceding reductive catalyst treatment at 400 °C or 300 °C. (d) Mössbauer spectra of Fe-CP-re400-s and Fe-TD-re400-s (300 mg of each catalyst were used for catalytic tests). The Mössbauer spectrum of Fe-SG-re400-s is given in Fig. S11. (e) Fraction of Fe-containing phases determined from the Mössbauer spectra in (d) and Fig. S11. (f) Spatially resolved fractions of Fe-containing phases in Fe-CP-re400-s and Fe-TD-re400-s determined from the Mössbauer spectra in Fig. S12. (g) Normalized Fe K-edge XANES spectra and (h) k^2-weighted Fourier-transformed EXAFS spectra of Fe-CP-re400-s and Fe-TD-re400-s located at the first upstream layer in (f).

in Fig. S20a. Based on the results of linear combination analysis (LCA) of XANES spectra, the Fe-TD-re400-s and Fe-CP-re400-s samples contain 97.5% and 66.1% of Fe_5C_2, respectively (Fig. S21). The only remaining phase is Fe_3O_4. Small differences in the fraction of Fe_5C_2 determined from analyzing Mössbauer spectra and LCA of XANES spectra (85.2% vs. 97.5% and 50% vs. 66.1%) of these materials can be due to experimental errors of each technique or data processing error. Corrections in the deconvolution of Mössbauer spectra are not always straightforward [49]. The precision of the LCA method depends on the quality of individual reference spectra used for fitting. Typically, the spectra are obtained by measuring the corresponding components. However, their structure (e.g., the presence of local or long-range defects, morphology) may be different from the structure of the analyzed samples. Nevertheless, both spectroscopic techniques identified a higher fraction of Fe_5C_2 in the Fe-TD-re400-s catalyst in comparison with that in the Fe-CP-re400-s catalyst.

In agreement with XANES data, the Fourier transformed k^2-weighted extended X-ray absorption fine structure (EXAFS) spectra of these samples are characterized by Fe-O and Fe-O-Fe scatterings like in Fe_3O_4 oxide and an additional Fe-C-Fe scattering associated with the Fe-C-Fe distance in Fe_5C_2 (Fig. 3h). The Fe-C scattering (between 1 and 2 Å) is much weaker in the intensity and overlapped by more intense Fe-O scattering. When these spectra are visually compared, it becomes obvious that the maximum of the Fe-C-Fe peak in the spectrum of Fe-CP-re400-s is shifted to a lower distance compared with that of Fe-TD-re400-s and Fe_5C_2 (Fig. 3h, Fig. S22). To derive an insight into the origin of such shift, we fitted the EXAFS spectra. All fitting details are given in Table S6. The average Fe-C-Fe distance in iron carbides of the

Fe-TD-re400-s and Fe-CP-re400-s materials is 2.613 Å and 2.579 Å (Table S6), respectively. Interestingly, the Fe-C-Fe distance of 2.613 Å for Fe-TD-re400-s is close to 2.615 Å determined for a Fe_5C_2 reference. Based on the results of XRD analysis of fresh and spent catalysts (Sections 3.1 and 3.4, Fig. S1 and Fig. S14), the significantly lower Fe-C-Fe distance for the Fe-CP-re400-s catalyst can indicate the presence of planar defects in the iron sublattice. Both Fe-CP fresh and spent catalysts are characteristic of a defective crystalline structure possessing packing disorders in the sublattice of iron along c direction.

Our LCA analysis of the XANES spectra of Fe-CP-re300-s and Fe-TD-re300-s (Fig. S23) identified Fe_3O_4 as the major phase in their first upstream layer (77.4% and 73.0%, respectively). The corresponding content of Fe_5C_2 is 22.6% and 27.0%. The Fe-O and Fe-O-Fe scatterings of Fe_3O_4 oxide are dominant in the EXAFS spectra that hinders the EXAFS fitting with Fe-C. Therefore, it is difficult to get reasonable results regarding the coordination number of Fe with respect to C. Nevertheless, the obtained fits (Table S6, Fig. S24) suggest the presence of low-intensity Fe-C-Fe scattering in Fe_5C_2. As for Fe-TD-re400-s and Fe-CP-re400-s, the iron carbides species in Fe-TD-re300-s and Fe-CP-re300-s differ in the Fe-C-Fe distance, which is also lower in the latter material due to the presence of planar defects in the iron sublattice in c direction as discussed above.

3.6. The ability of Fe_5C_2 to interact with CO_2, CO, and H_2

Temperature-programmed desorption tests with CO_2 (CO_2-TPD) revealed that CO_2 desorbs from spent catalysts between 400 and 750 °C (Fig. 4a, b; Table S7). The total CO_2 amount determined for the Fe-x-
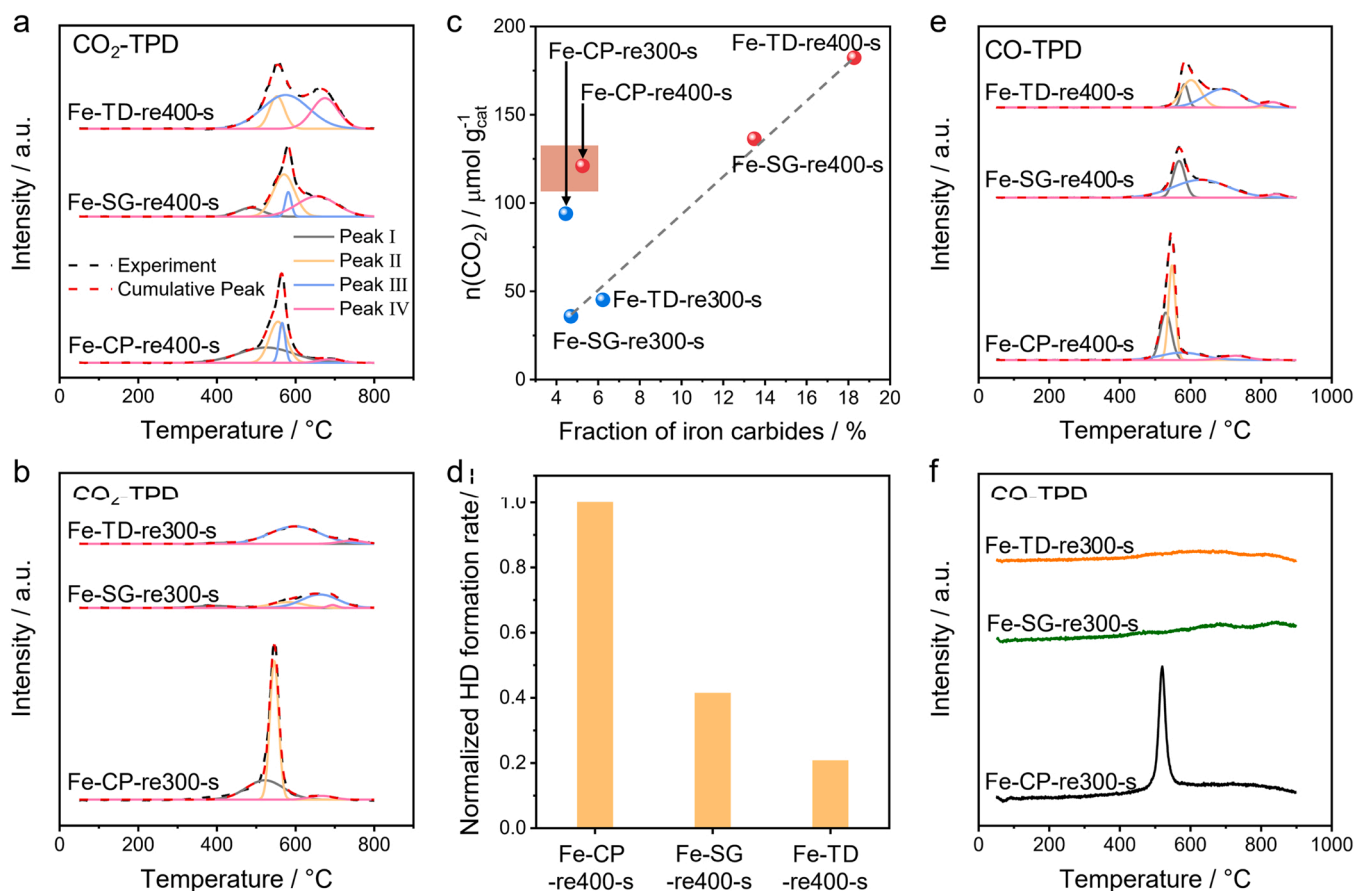

Fig. 4. CO_2 profiles collected in CO_2-TPD tests with (a) Fe-CP-re400-s, Fe-SG-re400-s, and Fe-TD-re400-s, as well as (b) Fe-CP-re300-s, Fe-SG-re300-s, and Fe-TD-re300-s. (c) The amount of CO_2 determined from the CO_2 profiles in (a, b) versus the fraction of iron carbides in the same catalysts. (d) The relative rate of HD formation over Fe-CP-re400-s, Fe-SG-re400-s, and Fe-TD-re400-s determined from H_2/D_2 exchange measurements. Temperature-programmed desorption profiles of CO of (e) Fe-CP-re400-s, Fe-SG-re400-s, and Fe-TD-re400-s, as well as (f) Fe-CP-re300-s, Fe-SG-re300-s, and Fe-TD-re300-s.

re400-s series catalysts decreases in the order Fe-TD-re400-s > Fe-SG-re400-s > Fe-CP-re400-s. For the Fe-x-re300-s series catalysts, the order changes to Fe-SG-re300-s < Fe-TD-re300-s < Fe-CP-re300-s. The Fe-x-re400-s series catalysts have higher concentration of CO_2 adsorption sites than the Fe-x-re300-s series catalysts.

To check if CO_2 adsorbs on Fe_3O_4 or Fe_5C_2/Fe_3C, CO_2-TPD tests were also performed with reduced catalysts containing Fe and Fe_3O_4 (Fig. S25), with the latter being the main component as in the spent catalysts (Fig. 3e). The concentration of CO_2 desorbed from reduced catalysts is significantly lower than that from their spent counterparts (Table S7, S8). Thus, we can safely conclude that Fe_5C_2 and Fe_3C adsorb CO_2 on the surface of spent catalysts. This conclusion is supported by a positive influence of the concentration of iron carbides in spent catalysts on the amount of CO_2 desorbed from these catalysts (Fig. 4c). Fe_5C_2 in Fe-CP-re400-s and Fe-CP-re300-s possesses higher concentration of CO_2 adsorption sites than Fe_5C_2 present in similar amounts in Fe-SG-re300-s and Fe-TD-re300-s. This result together with the maxima of CO_2 desorption and the fraction of differently strong adsorbing CO_2 species (Table S7) prove that Fe_5C_2 in Fe-CP spent catalysts differs from that in Fe-SG and Fe-TD spent catalysts in its ability to interact with CO_2. This statement is also valid for the ability of Fe_5C_2 to activate hydrogen (Fig. 4d).

We also investigated CO desorption from spent catalysts because adsorbed CO species are responsible for the formation of C_{2+}–hydrocarbons in the CO_2/CO-FT reactions. Fe-CP-re400-s was established to have higher concentration of CO adsorption sites than Fe-SG-re400-s and Fe-TD-re400-s (Fig. 4e, Table S9). Moreover, the sites for CO adsorption on the surface of Fe-CP-re400-s are more uniform as evidenced by the sharper CO desorption peak (Fig. 4e). The temperature

of the maximal CO desorption rate over Fe-CP-re300-s (520 °C) is lower than that over its counterpart, Fe-CP-re400-s spent catalyst (546 °C). It is worth noticing that no CO could be seen in the CO-TPD profiles of Fe-TD-re300-s and Fe-SG-re300-s (Fig. 4 f). Based on this result and on the fact that Fe_3O_4 is the main phase in the Fe-x-re400-s and Fe-x-re300-s catalysts, this iron oxide is not the main species adsorbing CO. Fe_5C_2 must be responsible for this process. Moreover, Fe_5C_2 in situ originated from Fe-CP strongly differs from that generated from the Fe-SG and Fe-TD catalysts in the ability to adsorb CO that is relevant for consecutive CO reactions.

3.7. Spatially resolved kinetic analysis

Having the above-mentioned structural and adsorptive characteristics of iron carbides in situ formed from Fe-CP, Fe-SG, and Fe-TD, we now analyze their reactivity for product formation in CO_2-FT. To this end, we performed CO_2-FT reaction tests using different amounts of fresh catalyst but keeping unchanged flow rate of feed. The segments are defined in Fig. 5a, and scaled between 0 and 1, with 1 standing for the highest catalyst amount of 300 mg. The segmental rates were calculated according to Eq. (4).

The highest CO_2 consumption rate was determined in the first about 2.5% upstream-located layer of all catalysts (Fig. 5b). In this regard, the catalysts follow the order of Fe-CP > Fe-SG >> Fe-TD. This rate decreases with the location of catalyst layer going to downstream (Fig. 5b). Such decrease was established to be strongest for Fe-CP. This distinguishing behavior in the spatially resolved CO_2 conversion rate probably relates to the different ability of the catalysts in CO_2 methanation, CO methanation, and/or CO-FT reaction. The latter two
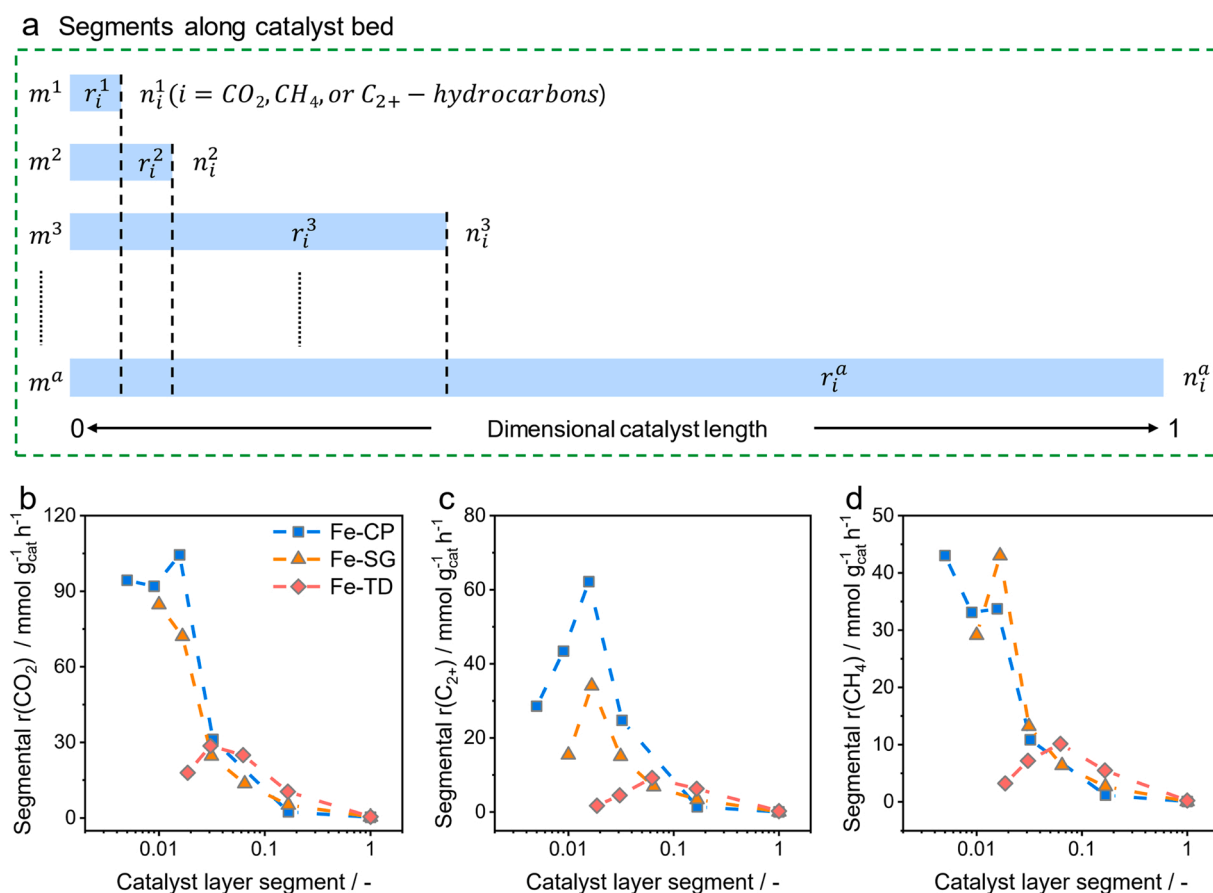

Fig. 5. (a) Graphical representation of segments along the catalyst bed. The segmental rates of (b) overall CO_2 conversion ($r(CO_2)$), (c) C_{2+}–hydrocarbons formation ($r(C_{2+})$), and (d) CH_4 formation ($r(CH_4)$) over Fe-CP, Fe-SG, and Fe-TD at 300 °C and 15 bar using a feed $H_2/CO_2/N_2 = 3/1/0.3$. The catalysts were initially reduced at 400 °C in 50 vol% H_2/N_2 for 2 h.

reactions are helpful for shifting the equilibrium of the RWGS reaction (the first step of CO_2-FT) into the forward direction that runs with the highest rate in course of CO_2-FT.

To check this assumption, we determined the segmental rate ($r(C_{2+})$) of C_{2+}–hydrocarbons formation (Fig. 5c). $r(C_{2+})$ reaches its maximum in the first 1.5–7% upstream-located layer depending on the used catalyst. This proves that C_{2+}–hydrocarbons are not the primary products in CO_2-FT but formed through CO-FT. The Fe-CP and Fe-SG catalysts have the highest $r(C_{2+})$ value in about 1.7% upstream-located layer. This high rate drops strongly in other downstream-located layers (Fig. 5c). In the contrast, the highest $r(C_{2+})$ over Fe-TD catalyst was determined at around 7% upstream catalyst bed position. Moreover, this high $r(C_{2+})$ can be kept within 17% catalyst layer. This catalyst also shows higher $r(C_{2+})$ in comparison with Fe-CP catalyst and Fe-SG catalyst below 17% upstream-located layer. Based on the spatial profiles of iron carbides in spent catalysts (Fig. 3 f), the efficiency of Fe-TD to produce C_{2+}–hydrocarbons in downstream located layers must be determined by the catalyst ability to stabilize iron carbides. They are, however, intrinsically significantly less active than those present in spent Fe-CP. This conclusion is made based on the fact that Fe-TD possesses a higher fraction of Fe_5C_2 in the upstream layer but shows lower rate of C_{2+}–hydrocarbons formation in this layer (Fig. 3f, Fig. 5c). Importantly, the size of Fe_5C_2 crystallites in all three spent catalysts is very similar even though the catalyst precursor materials are composed of differently sized Fe_2O_3 crystallites (Table S10). Therefore, the effect of the size of Fe_5C_2 crystallites on the formation rate of C_{2+}–hydrocarbons can be excluded.

The catalysts also show different activity in terms of CH_4 formation (Fig. 5d). The corresponding segmental rate ($r(CH_4)$) decreases along the catalyst bed because of transition from differential to integral reactor operation. This dependence also indicates that CH_4 is directly formed through direct CO_2 hydrogenation. This pathway plays a minor role over Fe-TD and Fe-SG with rising CO_2 conversion degree because $r(CH_4)$ goes through a maximum. Thus, CO is the main source of CH_4 over these two catalysts. Similar to $r(C_{2+})$, Fe-TD also shows higher $r(CH_4)$ in comparison with Fe-CP and Fe-SG after 7% upstream-located layer, however, at a very low level. This may be attributed to the presence of Fe_3C located between 30% and 50% catalyst layer (Fig. 3f).

3.8. Surface intermediates leading to CO or CH₄ and their lifetime

To further understand the origins behind the distinct activity of Fe-CP, Fe-SG, and Fe-TD in CO_2-FT (Fig. 5), steady-state isotopic transient kinetic analysis (SSITKA) was applied for determining the concentration of surface intermediates yielding CO and CH_4, as well as their lifetime.[36,37,50] SSITKA experiments were performed at 1.5 bar and 300 °C. The H_2/CO_2 ratio of 11 was employed to minimize the production of higher hydrocarbons as performed for CO-FT.[50] These reaction tests at atmospheric pressure should be representative for normal CO_2-FT reaction tests under high pressure because the distinct performance of these catalysts in CO_2 hydrogenation is not influenced by total pressure (Table S11).

The catalysts were initially exposed to a flow of $^{12}CO_2/H_2/Ar$ (volume ratio of 1/11/7) feed mixture until a steady-state operation was reached. Then, the reaction feed was changed to an isotopically labelled feed $^{13}CO_2/H_2/He/Ar$ (volume ratio of 1/11/0.5/6.5). After reaching a new steady-state performance with the latter feed, a back switch to the non-labelled feed was carried out. The normalized transient responses of ^{13}CO and $^{13}CH_4$ recorded in the back switch were collected and are displayed in Fig. 6a and Fig. 6b, respectively, with He response together. The catalysts follow the order of Fe-CP > Fe-SG > Fe-TD in terms of the difference between the ^{13}CO and He responses. The latter represents simple diffusion. An opposite order was determined for the $^{13}CH_4$ response.

According to the theory of SSITKA[37], the number of surface intermediates yielding CO or CH_4 (N_{CO} or N_{CHx}), as well as their lifetime (τ_{CO} or τ_{CHx}) were determined from the ^{13}CO and $^{13}CH_4$ transients. The τ_{CO} value decreases in the order of Fe-CP > Fe-SG > Fe-TD (Fig. 6c, d; Table S11). The N_{CHx} of Fe-CP is 1.04–2.37 times higher than those determined for the Fe-TD and Fe-SG catalysts (Fig. 6d). The rate of methane formation increases with an increase in the concentration of these species (Fig. S26) and with a decrease in their lifetime (Fig. 6c). Importantly, the lifetime of surface species leading to CH_4 is generally longer than that of those yielding CO. The ratio of τ_{CHx}/τ_{CO} for the Fe-CP, Fe-SG, and Fe-TD is 2.3, 3.9, and 9.7, respectively. The higher the ratio, the lower the activity for CO_2 methanation is (Fig. 2a, see the results of catalysts with reduction temperature of 300 °C).

Further insights into the kind of surface species leading to CO and CH_4 were derived from *in situ* Fourier-transform infrared spectroscopy (FTIR) experiments at 15 bar and 250 °C using a feed of $CO_2/H_2/He$ (1/3/1) and catalysts initially reduced at 400 °C (Fig. 6e, f). The bands at 2143 cm^{-1} and in the range of 1300–1900 cm^{-1} indicate the presence of gaseous CO and H_2O, respectively. This suggests that the RWGS reaction can occur over both catalysts. Carbonates- and formats-related IR bands could not be observed, probably due to their quick consumption into other gaseous products.

In agreement with steady-state catalytic tests (Fig. 5d), Fe-CP reveals higher activity towards CH_4 formation than Fe-TD (Fig. 6e, f; see the intensity of main bands centered at 3016 and 1305 cm^{-1} typical for gas-phase CH_4[51]). In comparison with a characteristic spectrum of CH_4, an asymmetry of the rotational bands of CH_4 in the spectrum of Fe-CP in the ν(C–H) region (Fig. 6e) is noticeable. Since C–H bands of other possible products can also be observed in this region, it seems that those bands are the reason for the asymmetry. To check this assumption, the spectrum obtained after 15 min on stream was subtracted from the others to obtain a partly compensation of the gas phase spectrum (Fig. S27). A δ(C–H) band (located at around 1470 cm^{-1})[52] can be observed in the spectrum of Fe-CP and the intensity of this band becomes stronger with an increase in time on stream in the same extent as the ν(C–H) band centered at about 2960 cm^{-1}. However, C-H bands (2917 and 2850 cm^{-1}) are quite weak in the non-compensated FTIR spectra collected over Fe-TD catalyst (Fig. 6 f). Therefore, there are differences in the kind and concentration of surface CH-containing species between these catalysts.

3.9. Structure-performance relationships

The above results demonstrate the importance of reducibility of α-Fe_2O_3 affected by the size of crystallites and the presence planner defects in the iron sublattice for (i) the *in situ* transformation into Fe_5C_2, Fe_3C (to a lesser extent), and Fe_3O_4 and (ii) the spatial distribution of these phases in the catalyst bed (Fig. 3 f). We confirmed that the presence of the defects in α-Fe_2O_3 is relevant for the formation of similarly defective structures in Fe_5C_2. The defectiveness of Fe_5C_2 seems to be essential for the generation of surface species from H_2, CO, and CO_2 (Fig. 4). Defective Fe_5C_2 originated from defective α-Fe_2O_3 was proven to possess more active sites for CO_2 and CO adsorption with medium adsorption strength than near to perfectly crystallized Fe_5C_2 originated from less defective α-Fe_2O_3 (Fig. S28, S29). This conclusion is indirectly supported by previous theoretical studies[53,54], highlighting the crucial role of surface defects for CO adsorption/activation. Redox properties of α-Fe_2O_3/Fe_3O_4 are suggested to be a descriptor for the stability of Fe_5C_2 against hydrogenation to CH_4 (Fig. S30, Fig. S31, Table S3) and for their ability to form surface intermediates with different binding energies (Fig. 6c, d; Fig. S32), as well as for H_2 activation (Fig. 4d).

These structural and adsorptive characteristics of α-$Fe_2O_3/Fe_3O_4/Fe_5C_2$ play an important role in CO_2-FT. The activity of Fe_5C_2 towards CO conversion into C_{2+}–hydrocarbons depends on reducibility of Fe_2O_3, from which Fe_5C_2 was formed (Fig. S33). This physicochemical catalyst property also correlates with the rate of generation of surface hydrogen species from H_2 (Fig. 4d) that is relevant for CH_4 formation from CO/
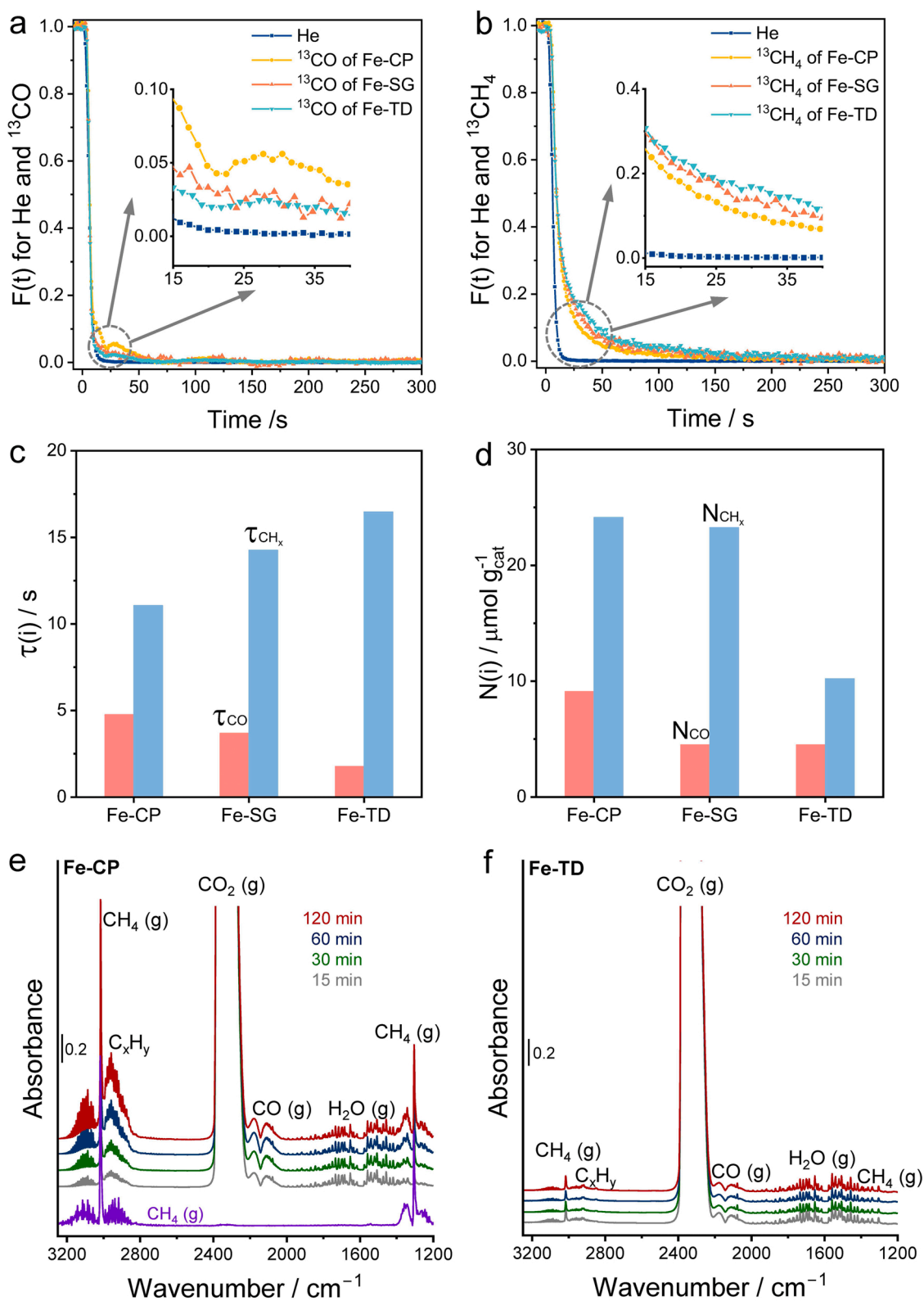
Fig. 6. Normalized transient responses of (a) He and ^{13}CO as well as (b) He and $^{13}CH_4$ of Fe-CP, Fe-SG, and Fe-TD obtained upon the back switch from the $^{13}CO_2/11\ H_2/0.5He/6.5Ar$ feed to the $^{12}CO_2/11\ H_2/7Ar$ feed at 300 °C and 1.5 bar. (c) The lifetime ($\tau(i)$) and (d) the number ($N(i)$) of surface intermediates yielding gas-phase CO or CH_4 in CO_2-FT at 300 °C at 1.5 bar over Fe-CP, Fe-SG, and Fe-TD. *In situ* time-resolved FTIR spectra collected during CO_2-FT reaction at 250 °C and 15 bar over (e) Fe-CP and (f) Fe-TD. The catalysts were initially reduced at 400 °C for 2 h. A typical gas-phase methane spectrum is shown in purple in (e).

CO_2. Thus, an interplay between the kinetics of generation and consumption of C- and H-containing surface fragments from CO/CO_2 and H_2, respectively, and their relative lifetime determine product selectivity in CO_2-FT. To support this statement, we use the ratio of the rates of formation of CH_4 and C_{2+}–hydrocarbons ($r(CH_4)/r(C_{2+})$). It decreases from 1.5 to 0.44, from 1.9 to 0.8, and from 1.9 to 0.9 with an increase in bed length of Fe-CP, Fe-SG, and Fe-TD from 0.5% to 3%, from 1% to 16%, and from 2% to 16%, respectively (Fig. S34). Importantly, the amount of Fe_5C_2 in all these layers is above 50%. The decrease should be related to an increase in CO partial pressure and a decrease in H_2 partial pressure along the catalyst bed (Fig. S35). Consequently, the fraction of surface C-containing species increases in expense of hydrogen species, which is favorable for C_{2+}–hydrocarbons formation and unfavorable for CH_4 formation. In the remaining 84% catalyst layer, the $r(CH_4)/r(C_{2+})$ ratio for Fe-CP and Fe-SG increases to 2.2, while no changes could be established for Fe-TD. The increase is explained by the absence of iron carbides and participation of Fe_3O_4 in CH_4 formation. Thus, for an efficient CO_2 hydrogenation to C_{2+}–hydrocarbons, an optimal ratio between Fe_3O_4 and Fe_5C_2 is required.

4. Conclusions

In summary, systematic investigations of the reaction-induced catalyst restructuring, spatial resolved distribution of iron-containing phases, and kinetic/mechanistic study (including spatial resolved under steady state and transient kinetic analysis with isotopic tracers) enabled us to disclose important factors influencing both activity and selectivity of Fe_2O_3-based catalysts in CO_2 hydrogenation. The reducibility is determined by the size of α-Fe_2O_3 crystallites and/or the presence of planar defects in the lattice of α-Fe_2O_3. The smaller the crystallites, the higher the defectiveness is and the higher the reducibility is. Our careful XRD and EXAFS analyses suggest that the presence of planar defects in α-Fe_2O_3 is relevant for the formation of similarly defective Fe_5C_2. The lower the concentration of the defects (large α-Fe_2O_3 crystallites), the higher the perfection of the crystalline Fe_5C_2 structure is. The structure of Fe_5C_2 is critical for its interaction with CO_2, H_2, and CO. Defective Fe_5C_2 favors efficient CO_2 and CO adsorption. Therefore, the catalytic performance (activity and product selectivity) in CO_2-FT is governed through controlling the reducibility of fresh iron oxide catalysts.

In an extreme case, when Fe_3O_4 dominates over perfectly crystallized Fe_5C_2 any hydrogenation of CO/CO_2 can be completely suppressed in CO_2-FT. The ratio between Fe_3O_4/Fe_5C_2 is tuned through reduction treatment of α-Fe_2O_3 before starting CO_2-FT. A near 100% CO selectivity was obtained at close to equilibrium degrees of CO_2 conversion. Hence, we have gained both fundamental and application relevant understanding that may be relevant for the development of efficient catalysts for CO_2 hydrogenation to CO exclusively or additionally CO hydrogenation to hydrocarbons.

CRediT authorship contribution statement

Qingxin Yang: Investigation, Methodology, Formal analysis, Writing – original draft, Writing – review & editing. **Elizaveta A. Fedorova:** Investigation, Formal analysis, Writing – review & editing. **Sergey A. Petrov:** Investigation, Formal analysis, Writing – review & editing. **Jana Weiss:** Investigation, Writing – review & editing. **Henrik Lund:** Investigation, Formal analysis, Writing – review & editing. **Andrey Skrypnik:** Investigation, Writing – review & editing. **Carsten Robert Kreyenschulte:** Investigation, Formal analysis, Writing – review & editing. **Victor Yu. Bychkov:** Investigation, Writing – review & editing. **Alexander A. Matvienko:** Investigation, Writing – review & editing. **Angelika Brueckner:** Funding acquisition, Writing – review & editing. **Evgenii V. Kondratenko:** Conceptualization, Supervision, Funding acquisition, Writing – review & editing.

Declaration of Competing Interest

The authors declare that they have no known competing financial interests or personal relationships that could have appeared to influence the work reported in this paper.

Data Availability

Data will be made available on request.

Appendix A. Supporting information

Supplementary data associated with this article can be found in the online version at doi:10.1016/j.apcatb.2023.122450.

References

[1] E.V. Kondratenko, G. Mul, J. Baltrusaitis, G.O. Larrazábal, J. Pérez-Ramírez, Status and perspectives of CO_2 conversion into fuels and chemicals by catalytic, photocatalytic and electrocatalytic processes, Energy Environ. Sci. 6 (2013) 3112–3135.

[2] W. Zhou, K. Cheng, J. Kang, C. Zhou, V. Subramanian, Q. Zhang, Y. Wang, New horizon in C1 chemistry: breaking the selectivity limitation in transformation of syngas and hydrogenation of CO_2 into hydrocarbon chemicals and fuels, Chem. Soc. Rev. 48 (2019) 3193–3228.

[3] D.H. Kim, J.L. Park, E.J. Park, Y.D. Kim, S. Uhm, Dopant effect of barium zirconate-based perovskite-type catalysts for the intermediate-temperature reverse water gas shift reaction, ACS Catal. 4 (2014) 3117–3122.

[4] X. Yang, X. Su, X. Chen, H. Duan, B. Liang, Q. Liu, X. Liu, Y. Ren, Y. Huang, T. Zhang, Promotion effects of potassium on the activity and selectivity of Pt/zeolite catalysts for reverse water gas shift reaction, Appl. Catal. B-Environ. 216 (2017) 95–105.

[5] C. Wang, E. Guan, L. Wang, X. Chu, Z. Wu, J. Zhang, Z. Yang, Y. Jiang, L. Zhang, X. Meng, B.C. Gates, F.-S. Xiao, Product selectivity controlled by nanoporous environments in zeolite crystals enveloping rhodium nanoparticle catalysts for CO_2 hydrogenation, J. Am. Chem. Soc. 141 (2019) 8482–8488.

[6] M. Juneau, M. Vonglis, J. Hartvigsen, L. Frost, D. Bayerl, M. Dixit, G. Mpourmpakis, J.R. Morse, J.W. Baldwin, H.D. Willauer, M.D. Porosoff, Assessing the viability of K-Mo_2C for reverse water–gas shift scale-up: molecular to laboratory to pilot scale, Energy Environ. Sci. 13 (2020) 2524–2539.

[7] C. Meng, G. Zhao, X.-R. Shi, Q. Nie, Y. Liu, Y. Lu, Electronic modulation of $InNi_3C_{0.5}/Fe_3O_4$ by support precursor toward efficient CO_2 hydrogenation to methanol, Appl. Catal. B-Environ. 316 (2022), 121699.

[8] Y. Xu, P. Zhai, Y. Deng, J. Xie, X. Liu, S. Wang, D. Ma, Highly selective olefin production from CO_2 hydrogenation on iron catalysts: a subtle synergy between manganese and sodium additives, Angew. Chem. Int. Ed. 59 (2020) 21736–21744.

[9] R. Yao, J. Wei, Q. Ge, J. Xu, Y. Han, Q. Ma, H. Xu, J. Sun, Monometallic iron catalysts with synergistic Na and S for higher alcohols synthesis via CO_2 hydrogenation, Appl. Catal. B-Environ. 298 (2021), 120556.

[10] L. Pastor-Pérez, F. Baibars, E. Le Sache, H. Arellano-García, S. Gu, T.R. Reina, CO_2 valorisation via reverse water-gas shift reaction using advanced CS doped Fe-Cu/Al_2O_3 catalysts, J. CO_2 Util. 21 (2017) 423–428.

[11] J. Castells-Gil, S. Ould-Chikh, A. Ramírez, R. Ahmad, G. Prieto, A.R. Gómez, L. Garzón-Tovar, S. Telalovic, L. Liu, A. Genovese, N.M. Padial, A. Aguilar-Tapia, P. Bordet, L. Cavallo, C. Martí-Gastaldo, J. Gascon, Unlocking mixed oxides with unprecedented stoichiometries from heterometallic metal-organic frameworks for the catalytic hydrogenation of CO_2, Chem. Catal. 1 (2021) 364–382.

[12] H. Chen, Z. Zhao, G. Wang, Z. Zheng, J. Chen, Q. Kuang, Z. Xie, Dynamic phase transition of iron oxycarbide facilitated by pt nanoparticles for promoting the reverse water gas shift reaction, ACS Catal. 11 (2021) 14586–14595.

[13] C.-Y. Chou, J.A. Loiland, R.F. Lobo, Reverse water-gas shift iron catalyst derived from magnetite, Catalysts 9 (2019) 773.

[14] W.-Z. Yu, X.-P. Fu, K. Xu, C. Ling, W.-W. Wang, C.-J. Jia, CO_2 methanation catalyzed by a Fe-Co/Al_2O_3 catalyst, J. Environ. Chem. Eng. 9 (2021), 105594.

[15] A. Parastaev, V. Muravev, E.H. Osta, A.J. van Hoof, T.F. Kimpel, N. Kosinov, E. J. Hensen, Boosting CO_2 hydrogenation via size-dependent metal–support interactions in cobalt/ceria-based catalysts, Nat. Catal. 3 (2020) 526–533.

[16] C. Yang, S. Liu, Y. Wang, J. Song, G. Wang, S. Wang, Z.J. Zhao, R. Mu, J. Gong, The interplay between structure and product selectivity of CO_2 hydrogenation, Angew. Chem. Int. Ed. 58 (2019) 11242–11247.

[17] Y. Li, X. Cai, S. Chen, H. Zhang, K.H.L. Zhang, J. Hong, B. Chen, D.-H. Kuo, W. Wang, Highly dispersed metal carbide on ZIF-derived pyridinic-N-doped carbon for CO_2 enrichment and selective hydrogenation, ChemSusChem 11 (2018) 1040–1047.

[18] F.-M. Sun, C.-F. Yan, Z.-D. Wang, C.-Q. Guo, S.-L. Huang, Ni/Ce–Zr–O catalyst for high CO_2 conversion during reverse water gas shift reaction (RWGS), Int. J. Hydrog. Energy 40 (2015) 15985–15993.

[19] M. Behrens, F. Studt, I. Kasatkin, S. Kühl, M. Hävecker, F. Abild-Pedersen, S. Zander, F. Girgsdies, P. Kurr, B.-L. Kniep, M. Tovar, R.W. Fischer, J.K. Nørskov, R. Schlögl, The active site of methanol synthesis over Cu/ZnO/Al industrial catalysts, Science 336 (2012) 893–897.

[20] S.-C. Yang, S.H. Pang, T.P. Sulmonetti, W.-N. Su, J.-F. Lee, B.-J. Hwang, C. W. Jones, Synergy between ceria oxygen vacancies and Cu nanoparticles facilitates the catalytic conversion of CO_2 to CO under mild conditions, ACS Catal. 8 (2018) 12056–12066.

[21] X. Zhao, H. Xu, X. Wang, Z. Zheng, Z. Xu, J. Ge, Monodisperse metal–organic framework nanospheres with encapsulated core–shell nanoparticles Pt/Au@Pd@ {Co_2(oba)$_4$(3-bpdh)$_2$}4H_2O for the highly selective conversion of CO_2 to CO, ACS Appl. Mater. Interfaces 10 (2018) 15096–15103.

[22] E. Sikora, Á. Prekob, G. Halasi, L. Vanyorek, P. Pekker, F. Kristály, T. Varga, J. Kiss, Z. Kónya, B. Viskolcz, Development and application of carbon-layer-stabilized, nitrogen-doped, bamboo-like carbon nanotube catalysts in CO_2 hydrogenation, ChemistryOpen 7 (2018) 789–796.

[23] J.H. Kwak, L. Kovarik, J. Szanyi, CO_2 reduction on supported Ru/Al_2O_3 catalysts: cluster size dependence of product selectivity, ACS Catal. 3 (2013) 2449–2455.

[24] J.C. Matsubu, V.N. Yang, P. Christopher, Isolated metal active site concentration and stability control catalytic CO_2 reduction selectivity, J. Am. Chem. Soc. 137 (2015) 3076–3084.

[25] S. Li, Y. Xu, Y. Chen, W. Li, L. Lin, M. Li, Y. Deng, X. Wang, B. Ge, C. Yang, S. Yao, J. Xie, Y. Li, X. Liu, D. Ma, Tuning the selectivity of catalytic carbon dioxide hydrogenation over iridium/cerium oxide catalysts with a strong metal-support interaction, Angew. Chem. Int. Ed. 56 (2017) 10761–10765.

[26] S. Kattel, W. Yu, X. Yang, B. Yan, Y. Huang, W. Wan, P. Liu, J.G. Chen, CO_2 hydrogenation over oxide-supported PtCo catalysts: the role of the oxide support in determining the product selectivity, Angew. Chem. Int. Ed. 55 (2016) 7968–7973.

[27] A. Ramirez, A. Dutta Chowdhury, A. Dokania, P. Cnudde, M. Caglayan, I. Yarulina, E. Abou-Hamad, L. Gevers, S. Ould-Chikh, K. De Wispelaere, V. van Speybroeck, J. Gascon, Effect of zeolite topology and reactor configuration on the direct conversion of CO_2 to light olefins and aromatics, ACS Catal. 9 (2019) 6320–6334.

[28] T. Riedel, G. Schaub, K.W. Jun, K.W. Lee, Kinetics of CO_2 hydrogenation on a K-promoted Fe catalyst, Ind. Eng. Chem. Res. 40 (2001) 1355–1363.

[29] E. de Smit, F. Cinquini, A.M. Beale, O.V. Safonova, W. van Beek, P. Sautet, B. M. Weckhuysen, Stability and reactivity of $\epsilon-\chi-\theta$ iron carbide catalyst phases in Fischer−Tropsch synthesis: controlling μ_c, J. Am. Chem. Soc. 132 (2010) 14928–14941.

[30] J.I. Orege, J. Wei, Y. Han, M. Yang, X. Sun, J. Zhang, C.C. Amoo, Q. Ge, J. Sun, Highly stable Sr and Na co-decorated Fe catalyst for high-valued olefin synthesis from CO_2 hydrogenation, Appl. Catal. B-Environ. 316 (2022) 121640.

[31] H. Yang, Y. Dang, X. Cui, X. Bu, J. Li, S. Li, Y. Sun, P. Gao, Selective synthesis of olefins via CO_2 hydrogenation over transition-metal-doped iron-based catalysts, Appl. Catal. B-Environ. 321 (2023), 122050.

[32] Q. Yang, A. Skrypnik, A. Matvienko, H. Lund, M. Holena, E.V. Kondratenko, Revealing property-performance relationships for efficient CO_2 hydrogenation to

[33] higher hydrocarbons over Fe-based catalysts: Statistical analysis of literature data and its experimental validation, Appl. Catal. B-Environ. 282 (2021) 119554.

[33] A.S. Skrypnik, Q. Yang, A.A. Matvienko, V.Y. Bychkov, Y.P. Tulenin, H. Lund, S. A. Petrov, R. Kraehnert, A. Arinchtein, J. Weiss, A. Brückner, E.V. Kondratenko, Understanding reaction-induced restructuring of well-defined $FexOyCz$ compositions and its effect on CO_2 hydrogenation, Appl. Catal. B-Environ. 291 (2021) 120121.

[34] P. Schouwink, L. Dubrovinsky, K. Glazyrin, M. Merlini, M. Hanfland, T. Pippinger, R. Miletich, High-pressure structural behavior of α-Fe_2O_3 studied by single-crystal X-ray diffraction and synchrotron radiation up to 25 GPa, Am. Mineral. 96 (2011) 1781–1786.

[35] J.J. Retief, Powder diffraction data and Rietveld refinement of Hägg-carbide, χ-Fe_5C_2, Powder Diffr. 14 (1999) 130–132.

[36] S. Reining, E.V. Kondratenko, N.V. Kalevaru, A. Martin, Steady-state and transient kinetic studies of the acetoxylation of toluene over Pd–Sb/TiO_2, ACS Catal. 6 (2016) 4621–4629.

[37] S.L. Shannon, J.G. Goodwin Jr, Characterization of catalytic surfaces by isotopic-transient kinetics during steady-state reaction, Chem. Rev. 95 (1995) 677–695.

[38] D. Gosset, C. Colin, A. Jankowiak, T. Vandenberghe, N. Lochet, X-ray diffraction study of the effect of high-temperature heat treatment on the microstructural stability of third-generation SiC, Fibers, J. Am. Ceram. Soc. 96 (2013) 1622–1628.

[39] G.N. Kryukova, S.V. Tsybulya, L.P. Solovyeva, V.A. Sadykov, G.S. Litvak, M. P. Andrianova, Effect of heat treatment on microstructure evolution of haematite derived from synthetic goethite, Mater. Sci. Eng., A 149 (1991) 121–127.

[40] M. Niederberger, F. Krumeich, K. Hegetschweiler, R. Nesper, An iron polyolate complex as a precursor for the controlled synthesis of monodispersed iron oxide colloids, Chem. Mater. 14 (2002) 78–82.

[41] L. Löffler, W. Mader, Anisotropic X-ray peak broadening and twin formation in hematite derived from natural and synthetic goethite, J. Eur. Ceram. Soc. 26 (2006) 131–139.

[42] P. Panagiotopoulou, A. Christodoulakis, D.I. Kondarides, S. Boghosian, Particle size effects on the reducibility of titanium dioxide and its relation to the water–gas shift activity of Pt/TiO_2 catalysts, J. Catal. 240 (2006) 114–125.

[43] Y. Zhang, Y. Zhao, T. Otroshchenko, H. Lund, M.-M. Pohl, U. Rodemerck, D. Linke, H. Jiao, G. Jiang, E.V. Kondratenko, Control of coordinatively unsaturated Zr sites in ZrO_2 for efficient C–H bond activation, Nat. Commun. 9 (2018) 3794.

[44] H.M. Torres Galvis, J.H. Bitter, T. Davidian, M. Ruitenbeek, A.I. Dugulan, K.P. de Jong, Iron particle size effects for direct production of lower olefins from synthesis gas, J. Am. Chem. Soc. 134 (2012) 16207–16215.

[45] J. Xu, C.H. Bartholomew, Temperature-programmed hydrogenation (TPH) and in situ Mössbauer spectroscopy studies of carbonaceous species on silica-supported iron Fischer− Tropsch catalysts, J. Phys. Chem. B 109 (2005) 2392–2403.

[46] E. de Smit, B.M. Weckhuysen, The renaissance of iron-based Fischer–Tropsch synthesis: on the multifaceted catalyst deactivation behaviour, Chem. Soc. Rev. 37 (2008) 2758–2781.

[47] P.P. Paalanen, S.H. van Vreeswijk, B.M. Weckhuysen, Combined in situ x-ray powder diffractometry/raman spectroscopy of iron carbide and carbon species evolution in Fe(−Na–S)/α-Al_2O_3 catalysts during Fischer–Tropsch synthesis, ACS Catal. 10 (2020) 9837–9855.

[48] L. Tang, L. He, Y. Wang, B. Chen, W. Xu, X. Duan, A.-H. Lu, Selective fabrication of χ-Fe_5C_2 by interfering surface reactions as a highly efficient and stable Fischer-Tropsch synthesis catalyst, Appl. Catal. B-Environ. 284 (2021), 119753.

[49] S. Li, R.J. O'Brien, G.D. Meitzner, H. Hamdeh, B.H. Davis, E. Iglesia, Structural analysis of unpromoted Fe-based Fischer–Tropsch catalysts using X-ray absorption spectroscopy, Appl. Catal. A-Gen. 219 (2001) 215–222.

[50] J.P. den Breejen, P.B. Radstake, G.L. Bezemer, J.H. Bitter, V. Frøseth, A. Holmen, K. P. de Jong, On the origin of the cobalt particle size effects in Fischer−Tropsch catalysis, J. Am. Chem. Soc. 131 (2009) 7197–7203.

[51] P.J. Linstrom, NIST Chemistry Webbook, https://webbook.nist.gov/2005.

[52] G. Socrates, Infrared and Raman Characteristic Group Frequencies: Tables and Charts, John Wiley & Sons, Chichester, 2004.

[53] C.-F. Huo, Y.-W. Li, J. Wang, H. Jiao, Insight into CH_4 formation in iron-catalyzed Fischer−Tropsch synthesis, J. Am. Chem. Soc. 131 (2009) 14713–14721.

[54] Q.-Y. Liu, C. Shang, Z.-P. Liu, In situ active site for CO activation in Fe-catalyzed Fischer–Tropsch synthesis from machine learning, J. Am. Chem. Soc. 143 (2021) 11109–11120.